Low-energy electron microscopy

by R. M. Tromp

Low-energy electron microscopy (LEEM) is a relatively new microscopy technique, capable of high-resolution (5 nm) video-rate imaging of surfaces and interfaces. This opens up the possibility of studying dynamic processes at surfaces, such as thin-film growth, strain relief, etching and adsorption, and phase transitions in real time, *in situ*, as they occur. The resulting video movies contain an unprecedented amount of information that is amenable to detailed, quantitative analysis. In this paper we discuss the principles of LEEM and its application to problems in science and technology.

Introduction

Low-energy electron microscopy (LEEM) was invented some 25 years ago by Ernst Bauer [1]. However, it would take almost two decades of isolated and painstaking development before imaging of surfaces with LEEM became a more or less routine reality [2]. The problems with bringing the invention to fruition related to the use of low electron energies (0–100 eV), the use of unconventional optics employing an electrostatic immersion objective lens, and the use of a folded beam path in which the electrons pass through the same objective lens field *twice*, necessitating the inclusion of a magnetic beam separator.

Before we get into the details of LEEM instrumentation, let us examine some images obtained using the technique. **Figure 1** shows four images obtained with our LEEM-I instrument [3], using four different imaging modes. Figure 1(a) is a photo-electron emission microscopy (PEEM) image of a molybdenum–disulfide sample. Such an image is obtained by illuminating the sample with ultraviolet light and using the photo-emitted electrons to form the image. Contrast is due to surface topography, as well as local changes in electron work function and/or electron density. The sample was cleaved with scotch tape. Freshly peeled regions emitted brightly, while contaminated areas were dark.

Figure 1(b) shows a different area on the same sample, imaged with an electron beam. The electrons do not actually reach the sample, but are made to reverse direction a few tens of nm in front of the sample. The resulting mirror electron microscopy (MEM) image is sensitive to topography as well as work function. The work function is the potential step from the metal Fermi level to the vacuum level. Local variations in work function give rise to local potential differences between the gun emitter and the sample surface, leading to different landing energies of the incoming electron beam. In addition, patchiness of the work function gives rise to fringing fields which locally deflect the incoming electron beam. The arrows in Figure 1(b) indicate stripes having a relatively low work function, most likely due to a composition fluctuation in the bulk of the sample that extends to the surface.

Figure 1(c) is a bright-field image of a Si(111) surface, at the (7×7)–(1×1) phase transition at ~860°C. The (7×7) structure refers to the well-known ordered reconstruction of the clean Si(111) surface [4] which is stable only up to 860°C, above which it becomes a disordered "(1×1)" structure. The term *bright-field* refers to the diffraction spot used for imaging. As in a transmission electron microscope (TEM), the electrons

©**Copyright** 2000 by International Business Machines Corporation. Copying in printed form for private use is permitted without payment of royalty provided that (1) each reproduction is done without alteration and (2) the *Journal* reference and IBM copyright notice are included on the first page. The title and abstract, but no other portions, of this paper may be copied or distributed royalty free without further permission by computer-based and other information-service systems. Permission to *republish* any other portion of this paper must be obtained from the Editor.

0018-8646/00/$5.00 © 2000 IBM

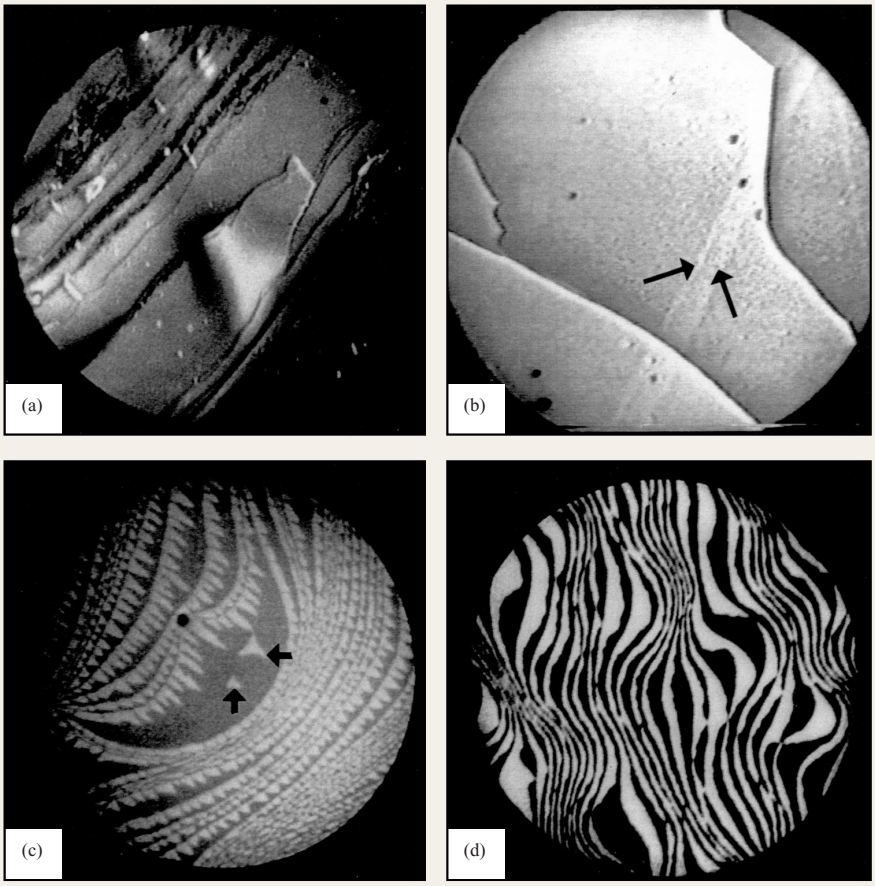

Figure 1

Images obtained in different imaging modes with a low-energy electron microscope: (a) Photo-electron emission microscopy image of a MoS_2 sample. Freshly cleaved areas are bright, others are dark. A delaminated area is seen near the center of the image. (b) Mirror electron microscopy image of the same sample. Cleavage steps are clearly seen, as well as differences in work function (indicated by arrows), probably due to small composition variations in the sample. (c) Bright-field low-energy electron microscopy image of the Si(111) (7×7)–(1×1) phase transitions. The (7×7) phase (bright) decorates the atomic steps during the phase transition, while the terraces are mostly covered by the (1×1) structure (dark). (d) Dark-field low-energy electron microscopy image of a Si(001)–(2×1) surface. The image was obtained with the (0, 1/2) diffraction spots reflected from every other terrace. Therefore, alternating terraces show up in bright, c.q. dark contrast, separated by 0.135-nm-high atomic steps.

undergo diffraction. At the low energies used in LEEM (0–100 eV), we obtain a low-energy electron diffraction (LEED) pattern, characteristic of the clean surface structure and symmetry. In a bright-field image, only the specular LEED (0, 0) beam is used to form the image. All other LEED spots are blocked by a contrast aperture. In Figure 1(c) we can see regions of the (7×7) structure (bright) and the (1×1) structure (dark). In addition, we can see the atomic steps on the surface, to which the (7×7) regions "adhere." Contrast is due to differences in the (0, 0) structure factor for the two phases. This figure is a single frame from a video showing the full dynamics of the phase transition, which is of first order, as can be seen directly from the coexistence of the two phases.

Figure 1(d) shows a dark-field image of a clean Si(001) surface, reconstructed in (2×1) dimer reconstruction [5]. Upon crossing an atomic step, the reconstruction rotates from (2×1) to (1×2). In a dark-field image one selects a diffracted beam *other* than (0, 0), in this case (1/2, 0). Thus, (2×1) terraces, diffracting into the (1/2, 0) beam, appear bright, while (1×2) terraces diffract into (0, 1/2) and appear dark. Dark-field imaging is a powerful tool for analyzing and imaging areas on the sample with different structure and symmetry.

Finally, we comment on the imaging of atomic steps and surface strain fields utilizing phase contrast. The electrons reflected from the surface form a plane wave field. At an atomic step, the plane waves reflected from the upper and lower terraces have different phases associated with them, since the step height is generally not exactly equal to an integer number of electron wavelengths. This phase difference can be made to show up directly in the image by slightly defocusing the objective lens, making the plane waves beat against each other [6]. An image showing atomic steps on Si(001) using phase contrast is shown in **Figure 2**. Phase contrast can also be used to image surface strain fields, due for instance to buried dislocations [7]. Thus, although the electrons do not penetrate deeply below the surface, LEEM can still "see" dislocations as far as 100 nm below the surface, because the dislocation strain fields extend to the surface of the sample. This is quite powerful in studies of strain relaxation phenomena in heteroepitaxial films [8].

LEEM instrumentation

The low electron energy in an LEEM instrument makes it unusually vulnerable to the deleterious effects of stray magnetic fields, hampering microscope alignment and degrading resolution. In the earliest LEEM instrument, use was made of a glass chamber [9], leaving it completely open to magnetic fields. Later, use was made of a stainless steel chamber, providing some shielding but still necessitating the use of dynamic field compensation coils to null out stray fields. The most modern LEEM instruments [10, 11] are engineered much like a transmission electron microscope, with magnetic lenses completely shielding the optical path. These instruments are compact and provide the highest spatial resolution.

An electrostatic immersion objective lens places the sample in a strong electrostatic field (up to 10 kV/mm for optimum resolution), putting stringent requirements on sample holder and stage design, in particular for experiments at high temperatures, and in the presence of atomic and/or molecular beams. The electrons traverse the focusing field of the objective lens (magnetic or electrostatic) at a relatively high electron beam energy (10–20 keV), and are decelerated between objective lens and sample to a final low energy of 0–100 eV (**Figure 3**). In this first pass, the "objective lens" functions as the final condenser, controlling the angle and location of illumination [12]. The electrons interact with and reflect

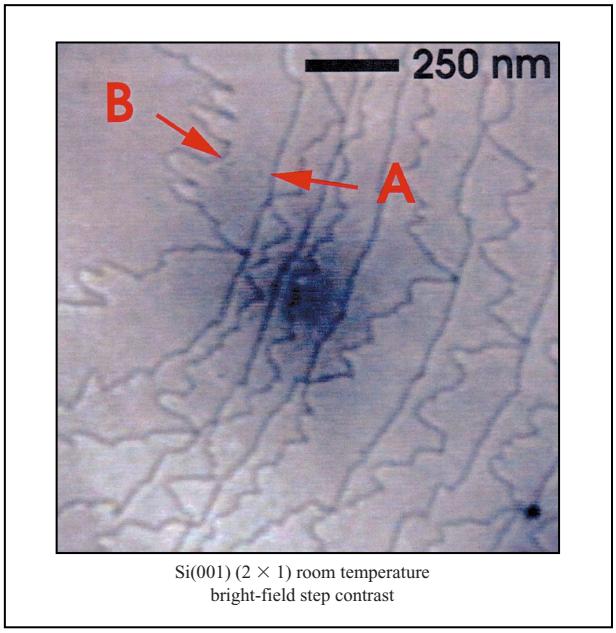

Si(001) (2 × 1) room temperature
bright-field step contrast

Figure 2

Bright-field LEEM image of a Si(001) (2 × 1) surface. Because all terraces diffract into the (0, 0) beam, there is no contrast difference between the terraces. However, the atomic steps can be seen because of a phase difference in the plane waves reflected from the terraces on either side of a step. Slight defocusing of the objective lens gives rise to Fresnel fringes at the step edge positions. A- and B-type steps are smooth and rough, respectively, due to a difference in atomic configuration.

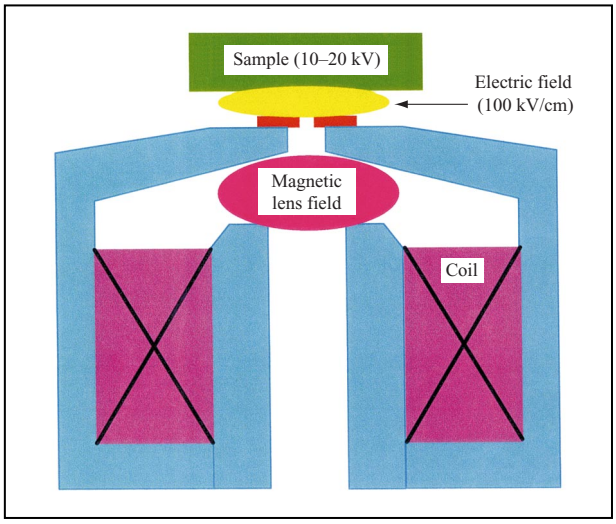

Figure 3

Schematic diagram of the objective lens of LEEM. The sample is maintained at a potential close to that of the electron source, decelerating the electrons in the strong electrostatic field between the objective anode aperture (red) and the sample to an energy of 0–100 eV. The magnetic lens field inside the objective lens acts both as the final condenser lens and as an image-forming lens. It is generated by the electromagnetic coil, placed inside the permendur lens housing (blue). The magnetic field does not extend to the sample itself.

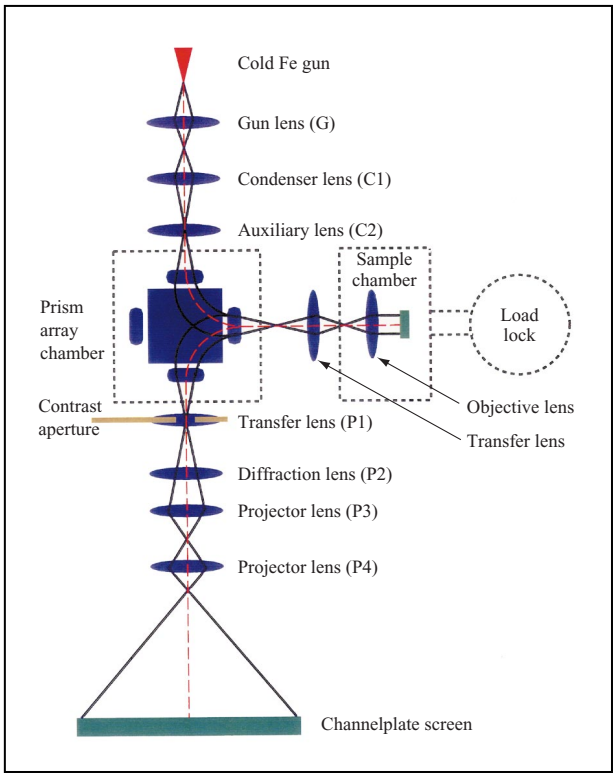

Figure 4

Schematic ray diagram of the LEEM-II instrument. Condenser and projector systems are separated by prism array, which relays electron beam to and from objective lens and sample chamber.

from the sample at a low energy, to be re-accelerated to the gun energy on their return to the objective lens. To accomplish this, the sample is maintained at a potential close to that of the electron emitter in the gun, while the objective lens is at ground potential. (Alternatively, the sample can be maintained at ground potential and everything else maintained at a high voltage [13].) The electrons then traverse the objective lens focusing field a *second* time to form a real image of the sample. The uniform electrostatic field between objective lens and sample accounts for most of the microscope's performance. It forms the first, virtual image in the microscope, at 2/3 magnification *behind* the sample [14]. The spherical and chromatic aberrations of this uniform immersion field are larger than those of any of the other lenses (if they are carefully designed), and therefore control the ultimate performance. Higher field strength translates into higher resolution, but the field strength is limited to about 10 kV/mm by electric breakdown across the sample–objective lens gap. The only controllable factor is the energy spread of the electron gun. For a hot emitter with a typical energy spread of 0.75 eV, the ultimate lateral resolution achievable is 8–10 nm; for a cold-field emitter with an energy spread of 0.25 eV, a 3–4-nm resolution is achievable, assuming that there are no other factors compromising the resolution (such as stray magnetic fields, vibrations, or additional aberrations from the objective lens or the beam separator). The objective lens aberrations (i.e., the combined aberrations of the electrostatic immersion field and the electrostatic or magnetic objective lens) are remarkably resistant to improvement. The effects of spherical and chromatic aberration, as well as diffraction (the maximum diffraction vector transmitted by the contrast aperture limits the minimum observable feature size), are roughly equal, unlike transmission electron microscopes, in which the resolution is dominated by spherical aberration. Without aberration correction, 3 nm appears to be a firm lower limit on the achievable LEEM resolution.

A magnetic beam separator is necessary to spatially separate the (illuminating) gun and condenser optics, and the (imaging) projector optics. This sounds rather trivial, but it is not. Consider a uniform magnetic field: It will deflect electrons traveling in a plane orthogonal to the field axis, but it leaves electrons traveling parallel to the field unaffected. In other words, it focuses *only* in the direction of deflection. This is not good. Ideally, the separator behaves like a round lens (or a series of round lenses). Until recently such a separator did not exist. The early LEEM instruments used a design by Archard and Mulvey [15], consisting of a uniform magnetic field over a circular region, with a strategically placed D-shaped cutout. To zeroth order this separator is nonfocusing, behaving like a drift space. In practice this design behaves like an astigmatic lens, with a (fortunately) long focal length. Images obtained with the separator show a tolerable but discernible image distortion due to unequal in-plane and out-of-plane magnifications, after correction of the astigmatism with the objective lens stigmator. The situation was improved with the introduction of so-called magnetic prism arrays by Kolarik et al. [16], based on the observation that two different magnetic fields are separated by a fringe field. If the electrons pass through this fringe field at an angle, there is a component of deflection in the out-of-plane direction. This makes it possible to obtain both in-plane and out-of-plane focusing. The challenge then is to design a separator containing multiple magnetic fields that is double-focusing, behaving like a series of round lenses. The first magnetic prism array was incorporated in a microscope designed by Veneklasen [10]. The deflection angle was 60°. This prism array was double-focusing for the image planes, but not for any other planes. In an electron microscope one always wants to faithfully transfer both the image *and* the diffraction planes, which are widely separated in space.

Thus, while the image is deflected without distortion, the diffraction pattern is not. In his thesis Degenhardt [17] showed that two nested, square magnetic fields can be used to form a truly double-focusing separator at a deflection angle of 90°. However, this design leaves no room for independent field adjustment on the condenser and projector sides needed to compensate for imperfections in manufacturing. Recently we introduced a hybrid between the prism array and the nested quadratic field design that is truly double-focusing for any pair of image/object planes [11]. That is, both the image and the diffraction planes are deflected and transferred at unit magnification, without distortion. Additionally, the image plane is free of energy dispersion, and, because of the inclusion of a rotation-free objective lens doublet, so is the diffraction pattern.

Figures 4 and **5** show a schematic ray diagram and CADAM drawing of our newest microscope, designated as LEEM-II (commissioned in early 1998). It achieves a lateral resolution of 5 nm, the highest resolution obtained with LEEM to date. The microscope features a cold-field-emission electron gun, with an energy spread of ~0.25 eV. It has two condenser lenses as well as an auxiliary condenser lens (for spot-mode and convergent beam operation); it uses the 90° deflection double-focusing prism array discussed above; it has a rotation-free objective lens doublet and a total of five lenses in the projector column (transfer lens, diffraction lens, and three projector lenses). In addition to these optical elements, there are two sets of stigmators in the condenser lens system, as well as three sets of steering coils. The objective lens contains a set of stigmators, and the projector column contains a set of steering coils. All of the electron lenses, stigmators, and steering coils are under computer control, as is the electron gun. The contrast aperture is placed at the center of the transfer lens in the projector column, where the LEED pattern is refocused by the separator. This allows dark-field imaging with any LEED spot within the first Brillouin zone. Selective area apertures are placed in the center plane of the separator where the Gaussian sample image is in focus. The final image, with magnification 400–100 000×, is displayed on a channelplate-intensified phosphor screen and recorded with a CCD camera.

The sample is mounted in a double-insulated ceramic holder with electron beam heating capability. Samples can be heated up to 1400°C for extended periods of time, while imaging. During imaging the sample can be exposed to atomic or molecular beams, up to pressures of 10^{-5} Torr. The sample "cap," a small Mo holder in which the sample is placed, can be exchanged without breaking vacuum. The sample holder is mounted on a piezoelectrically driven stage with three translations and two rotations, allowing accurate sample alignment, inspection over large areas (up to 6 mm diameter), and adjustment of the sample/objective lens distance.

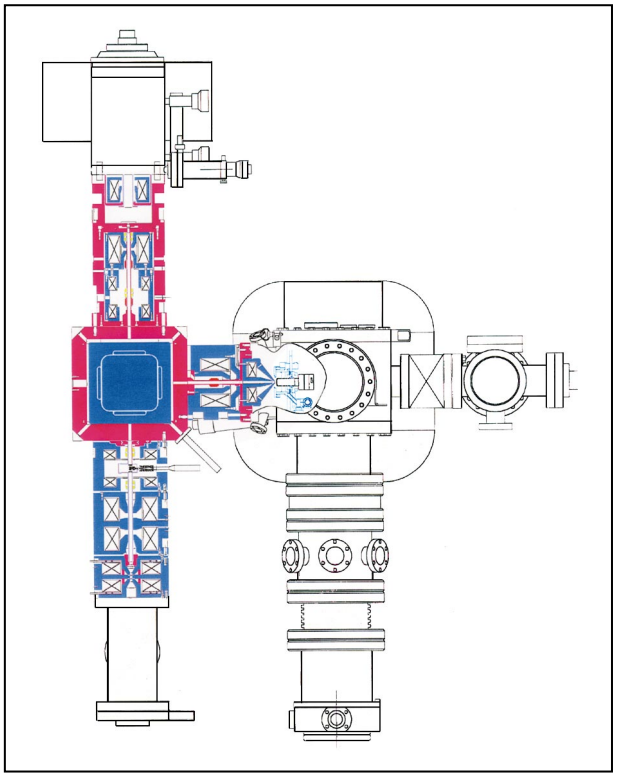

Figure 5

Simplified CADAM cross-sectional view of the LEEM-II instrument. Magnetic lenses are indicated in blue, nonmagnetic lens housings in red, and stigmators and steering coils in green.

The entire microscope is designed in accordance with ultrahigh-vacuum standards. The base pressure in the sample chamber is 2×10^{-10} Torr, and the electron gun pressure is about a factor of 10 lower to ensure stable tip operation. Over an eight-hour period, the tip emission current decays by less than 20% at constant extraction voltage. After evacuation the microscope is baked at 150°C to obtain the best possible vacuum. The sample position is surrounded by eight vacuum flanges for evaporators, gas sources, and ultraviolet illumination. A photograph of the LEEM-II instrument is shown in **Figure 6**.

Applications

We next discuss three different applications of LEEM in our laboratory. First we describe the dynamical study of a second-order phase transition, an example of some of the most basic science work we have done [18]. This work

Figure 6

Photograph of the LEEM-II instrument.

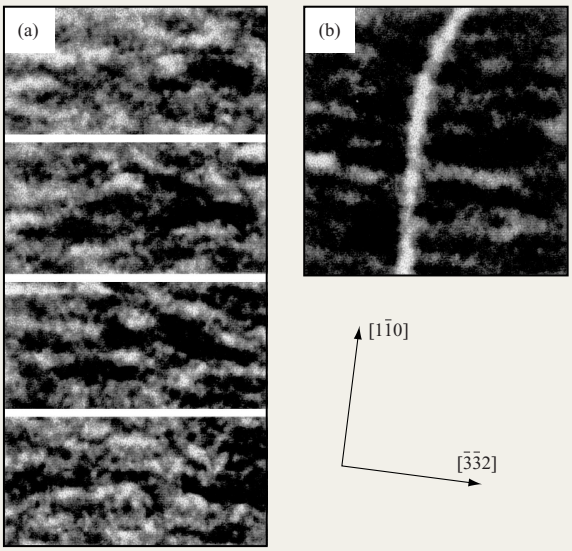

Figure 7

(a) Sequence of images of Si(113) near the second-order phase transition at 693°C, obtained upon cooling from the disordered state. Each (0.5-μm × 1-μm) image was obtained after a duration of 0.4 s and averaged over the previous 0.4 s. Extended correlations are clearly seen in the [$\bar{3}\bar{3}$2] direction. (b) A 1-μm-square image of the intensity near T_c crossed by a step bunch (light vertical line). There are no correlations in image intensity across this step bunch.

highlights the quality of real-time data obtainable with LEEM, and the detailed quantitative analysis that it makes possible. We then discuss the growth of Ge on Si(001) with and without the use of a surfactant monolayer [19]. Without a surfactant, Ge grows only to a thickness of three monolayers before islanding begins. With a surfactant, islanding can be completely suppressed. The LEEM studies show that the growth mode is very different in these two cases, suggesting a mechanism for the action by the surfactant on the surface. Finally, we discuss the imaging of hot-electron emission by MOS structures [20]. These studies are related to the reliability of thin gate oxides, and have given rise to a new lithography method, hot-electron emission lithography (HEEL), that we have recently developed [21].

- *The Si(113) (3 × 1) disorder phase transition*

At room temperature the Si(113) surface is reconstructed in a (3 × 1) superstructure. The detailed atomic nature of this reconstruction was determined on the basis of scanning tunneling microscopy observations by Dabrowski et al. [22]. At 693°C the surface undergoes a reversible transition to a disordered phase. Studies of the diffracted beam profiles with LEED [23] as well as X-ray diffraction [24] have shown that this is an example of a second-order phase transition, analogous to the transition from ferromagnetic to paramagnetic in a magnetic material.

Unlike a first-order transition—such as the Si(111) (7 × 7)–(1 × 1) transition of Figure 1(c)—a second-order phase transition shows no phase coexistence at the transition temperature. Instead, as the transition temperature is approached, "critical" fluctuations occur. Cooling down from the disordered phase, the free-energy cost of (3 × 1) domains becomes smaller as the transition temperature T_c is approached. Such unstable (3 × 1) domains fluctuate into and out of existence, with larger domain sizes closer to the transition temperature ("divergence of the coherence length"). Similarly, the domains become more stable and survive longer closer to the transition temperature ("critical slowing down"). Critical fluctuations are usually studied by diffraction techniques, although they can be observed directly in a

liquid as critical opalescence [25]. On Si(113) they can be observed directly with LEEM. **Figure 7** shows a sequence of images near the transition temperature, clearly indicating the fluctuations. Shown in the figure are single frames from a video recording; the full recordings can be used for a quantitative analysis. Using such images, we can measure the *intensity* of the fluctuations. Theory shows that their magnitude is proportional to the specific heat, diverging at the transition temperature. **Figure 8** shows this divergence, fitted with the expected power-law behavior, in agreement with previous diffraction measurements [18]. Using diffraction, it has not been possible to obtain the time structure of the fluctuations. According to renormalization group theory, the coherence length ξ is related to the fluctuation time constant τ by $\xi = \tau^z$, where z is the dynamical critical exponent [26]. The coherence length can be measured from the images by determining the dominant length scale of the fluctuations, and τ can be obtained by performing a time–time correlation analysis over a large number of video frames. **Figure 9** shows the relation between ξ and τ, and a fit using $z = 1.9$. A value of z close to 2 is predicted by renormalization group theory for a nonconserved order parameter, while a value close to 4 is predicted for a conserved order parameter. A value of $z = 1.9$ indicates that the number of atoms in the (3×1) and the disordered structures are not the same, with the atomic steps acting as sources and sinks of atoms. By imaging fluctuations on both sides of the atomic steps, we have also determined that the fluctuations are uncorrelated across a step. This limits the maximum coherence size, i.e., the divergence at T_c.

The analysis presented here relies on an extensive video record, with high-quality data over a range of temperatures and time scales. To establish a fluctuation time constant τ of one second, about 15 seconds of video is required, i.e., about 100 million pixel intensities for an analyzed area of 480 × 480 pixels. In a study of thermal step edge fluctuations on Si(001), we have analyzed about 40 million step edge positions (fitted to a data set that contained about four billion pixels) to obtain data on step free energies, stiffnesses, and mobilities. Clearly, these are not trivial tasks, impossible without modern video handling and computation facilities. But these massive data sets contain information not obtainable by any other means, and the result is well worth the effort.

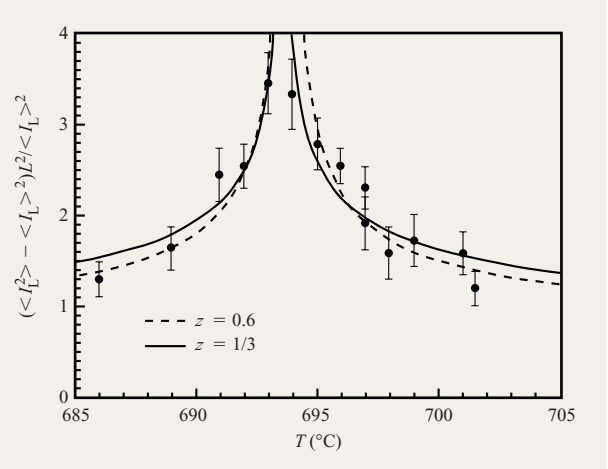

Figure 8

Time average of the mean square fluctuations in image intensity of 170-nm-square regions of the surface as a function of T. The peak near 693°C locates the critical point. L^2 is in units of the unit cell area, i.e., 1.27 nm × 1.15 nm. The fits are for two values of the critical exponent.

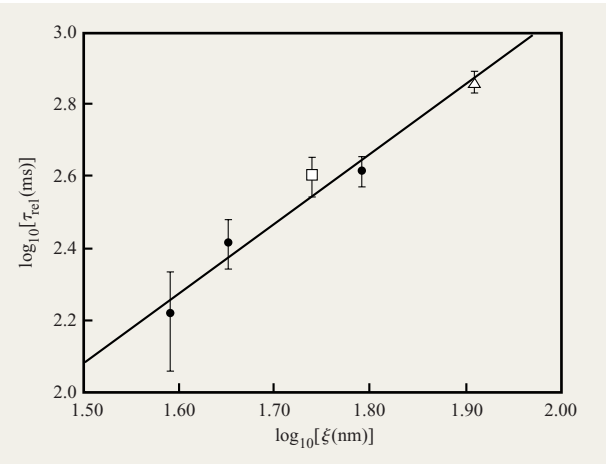

Figure 9

Log–log plot of the relaxation time τ_{rel} versus the correlation length ξ obtained from a detailed analysis of data such as shown in Figure 7. The fitted line is obtained for a critical exponent $z = 1.9 \pm 0.3$, where τ_{rel} is proportional to ξ^z.

- *The growth of Ge on Si(001)*

Suppose we grow a material B on a substrate A. If the surface free energy of B is smaller than that of A, i.e., $\sigma_B < \sigma_A$, B will wet A and form a continuous film. This is the conundrum of trying to grow an A/B/A/B/A/B . . . superlattice: If B wets A, A does not wet B. Reality is even worse. Even if $\sigma_B < \sigma_A$, B does not always form a continuous film. For instance, Ge wets Si(001). But the Ge lattice constant is about four percent larger than that of Si, and misfit strain causes islanding beyond the critical thickness. The critical thickness is only three atomic layers. The problem can be overcome by growing at low

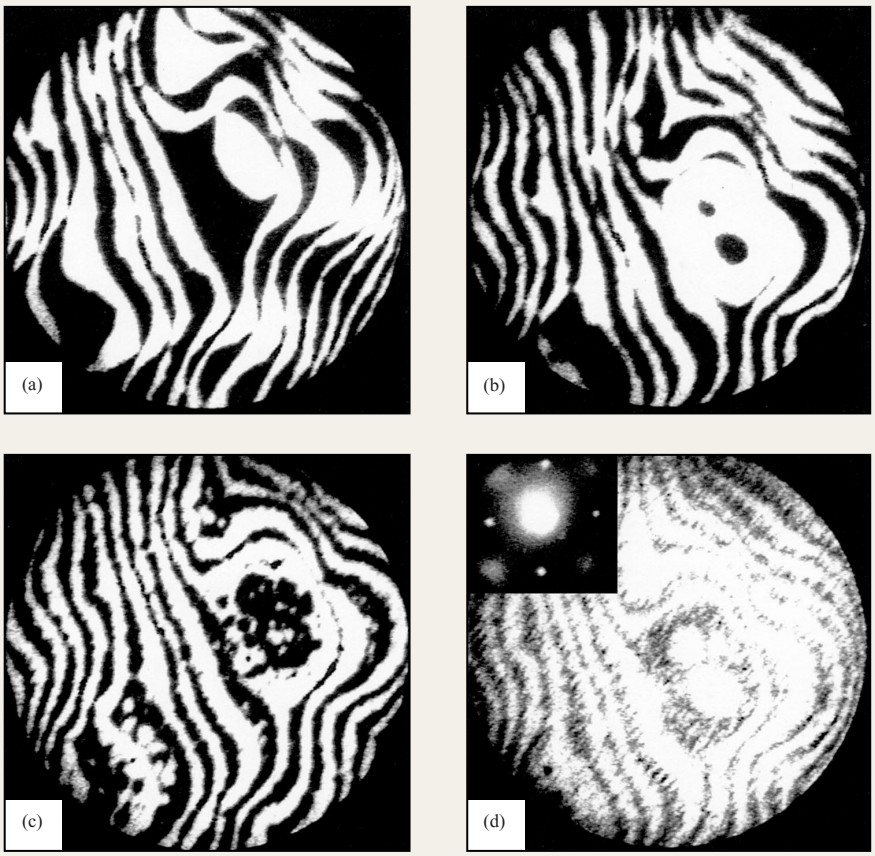

Figure 10

Dark-field LEEM images of Ge growth on a clean Si(001) surface, in the absence of a surfactant: (a) Starting surface. (b) After growth of about one monolayer of Ge. The surface is still smooth, with growth mostly occurring by step flow. Nucleation is seen on the large white terrace near the center. (c) After growth of about two monolayers of Ge. The step edges are becoming rough, and nucleation is now much more prevalent. (d) After growth of about three monolayers of Ge. Step flow is now almost absent, with dense nucleation on the terraces and rapidly evolving surface roughness. The diffraction pattern (inset) shows broad diffraction features in the <001> directions which are absent on the smooth starting surface.

temperature so that islanding is kinetically suppressed, but this also suppresses the kinetics of atom incorporation, and hence crystal quality. Using medium-energy ion scattering (see the paper by M. Copel in this issue [27]), we found in 1989 that there is another, more elegant solution to the problem [28]. Si prefers to be fourfold-coordinated. Atoms in the Si(001) surface have only two bonds to the substrate, and one dimer bond to their surface neighbors. There is one dangling bond left, leading to a high surface energy. If we could magically change the valency of Si to 5 rather than 4, the dangling bond would change to a fully occupied lone-pair orbital, chemically inert and low in energy. Chemistry allows such magic: Replace Si with As or Sb. The surface forms As or Sb dimers, with a considerably reduced energy. When we now try to grow Si or Ge on the surface, the As or Sb monolayer segregates with great efficiency, floating on top of the growing film. Even better, Ge no longer forms islands on Si, and vice versa. This happens at normal growth temperatures that ensure excellent crystal quality. Indeed, the best Si/Ge superlattices [29] have been grown with Sb as a "surfactant" (i.e., surface-active species). Fully relaxed, defect-free Ge films have been grown on Si(111) with electron mobilities that are as high as those of bulk Ge [30]. So how do the As or Sb surfactants work?

Figure 10 shows a sequence of images obtained during the growth of Ge on Si, without a surfactant [19]. The first layer grows smoothly. The second layer shows significant

roughening of the step edges. During growth of the third layer, the image loses contrast, indicative of a rough surface. Beyond the third layer, island growth sets in. (This is a subject in its own right. See the chapter on Ge quantum dot growth in the paper by F. Ross in this issue [31].) The diffraction pattern shows diffuse intensity in the ⟨010⟩ directions indicative of faceting. In contrast, **Figure 11** shows the progression of growth in the presence of a monolayer of As on the starting surface. At about one half monolayer of Ge coverage, the contrast virtually disappears, indicating a roughened surface. But at one monolayer of coverage the contrast recovers, albeit inverted from the initial contrast. This is a classical case of layer-by-layer growth: dense 2D island nucleation on the terraces, coalescence of the islands, and recovery of a smooth surface at a thickness of one monolayer. This process repeats layer after layer, with the As monolayer "floating" on the surface! The dense nucleation on the terraces indicates that the Ge atoms do not diffuse very far before they are incorporated into the substrate. The floating of the As is attributed to the fact that the energy of Ge on top of As is so much higher than that of As on top of Ge (more than 2 eV per unit cell [28]) and that site exchange is rapid and efficient. Once the Ge is below the As, it cannot return to the surface. Island formation is thus circumvented! This also occurs when Si grows on Ge. The surfactant monolayer changes the kinetics of atom incorporation. This change in kinetics is driven by the fact that the surfactant-terminated surface is thermodynamically extremely favorable.

Surfactants have now been used in a broad variety of growth systems besides Si/Ge—III–Vs [32] and II–VIs [33], metallic [34] and magnetic [35] superlattices, using a wide variety of surfactant elements. In biology, growth modifiers are found to play a key role in the growth of shells [36]. There the surface-active agents are much more complicated proteins, but they still affect the incorporation step, stabilizing one crystal structure over another. In all likelihood we are just at the tip of the iceberg regarding the use of additives to stabilize specific structures over others. The manipulation of energies with such surfactants provides a pathway to the assembly of new man-made structures and materials against thermodynamic odds.

• *Hot-electron emission from MOS structures*

Gate oxides are at the heart of silicon technology. As gate oxide thicknesses of 2 nm are rapidly approached, reliability becomes a serious concern [37]. The lifetime of an MOS device is limited by the maximum amount of charge that can flow from substrate to gate, the charge to breakdown, Q_{BD}. With a bias voltage applied to the gate, electrons tunnel from the substrate to the gate, an effect absent in thicker oxides. This tunneling current detracts

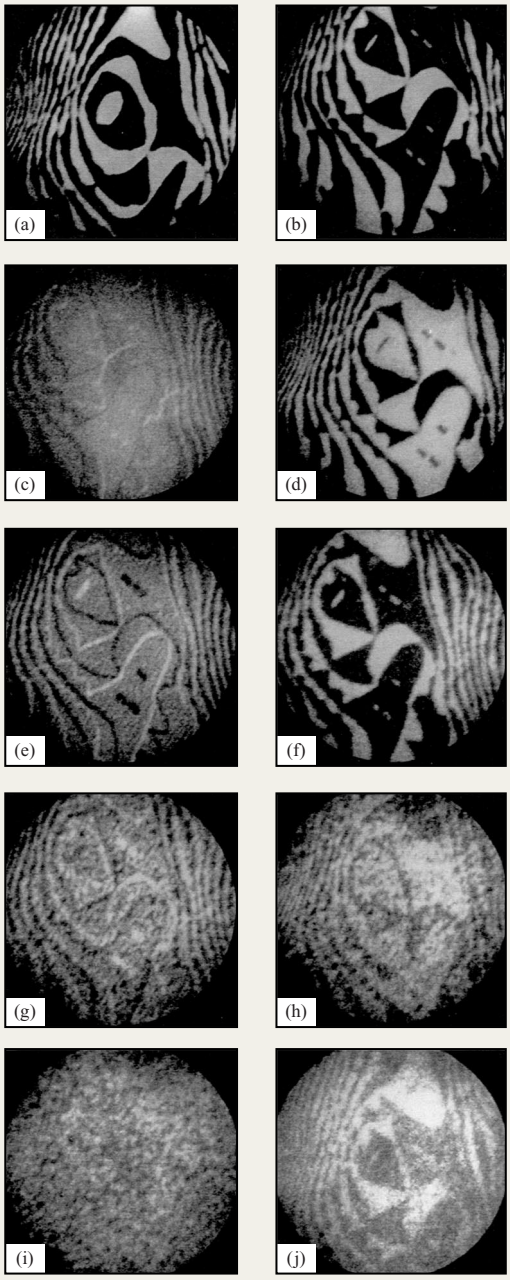

Figure 11

Growth of Ge on Si(001) in the presence of a monolayer of As on the starting surface: (a) Starting surface. (b, d, f, h, j) Surface with, respectively, one, two, three, and four monolayers of Ge. (c, e, g, i) Surface with, respectively, 0.5, 1.5, 2.5, and 3.5 monolayers of Ge. Dense nucleation is seen at fractional monolayer coverages, where contrast disappears almost completely, but at full monolayer coverage contrast reappears, indicating recovery of a smooth surface morphology. With the addition of each full monolayer of Ge the contrast inverts, as expected theoretically for smooth layer-by-layer addition.

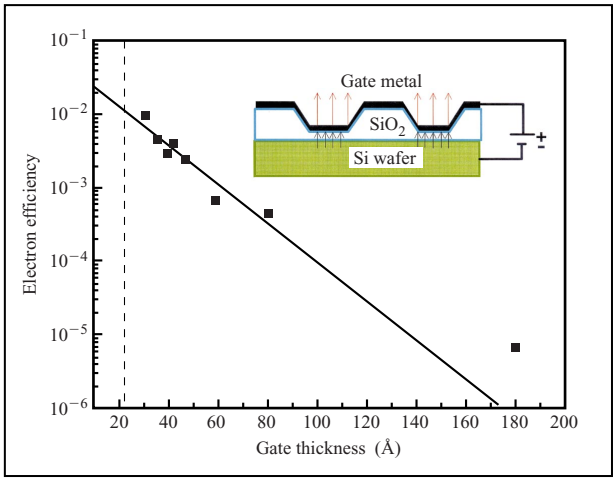

Figure 12

Electron emission efficiency (defined as the ratio of the electron current emitted into vacuum to the electron current tunneling from substrate to gate) for an MOS device having a thin gate oxide and thin gate, as a function of gate metal thickness. The gate was a thin Al film deposited onto SiO_2 at about 100 K. Below a thickness of 2 nm, the Al was discontinuous. The inset shows the sample geometry used [also used in hot-electron emission lithography (HEEL), discussed in the next section].

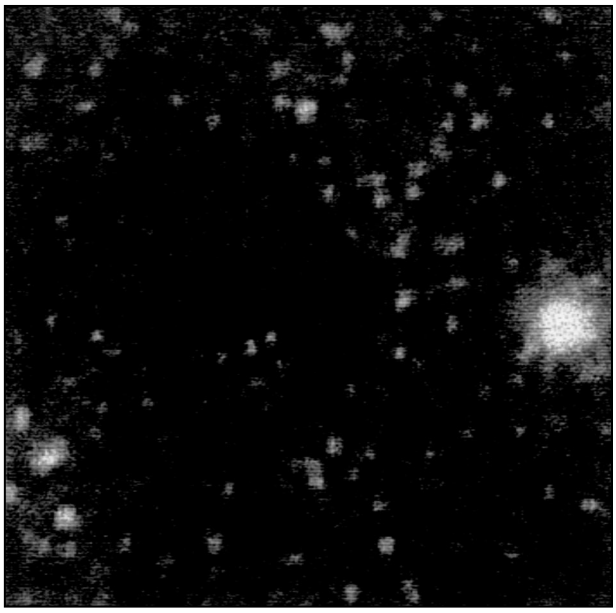

Figure 13

Hot-electron emission image, over a field of view of 25 μm, from a 7-nm-thick oxide biased at 9 V. Strongly nonuniform emission is observed as local breakdown phenomena give rise to local "hot spots" in the emission current.

from the lifetime and eventually poses a limit on the minimum oxide thickness that can be used in the device. There have been many studies of gate oxide breakdown phenomena, but there have been no real-time microscopy studies of the breakdown process. LEEM is an excellent method for performing such studies.

In a normal LEEM experiment, the electrons that form the image impinge on the sample from an electron gun, and are then reflected back toward the objective lens. PEEM shows us that we can also use electrons generated by the sample. Some years ago, Kolarik et al. showed that electron tunneling can occur from biased metal–insulator–metal (MIM) junctions into the vacuum [38]. Similar effects can be observed with metal–oxide–semiconductor (MOS) junctions. With the gate biased positive relative to an n-type substrate, electrons tunnel from substrate to gate. As the electrons ballistically traverse the oxide, they heat up in the applied field, and enter the gate electrode with a significant amount of kinetic energy. If the gate electrode is sufficiently thin, a small fraction of the electrons can pass through it unscattered and eject into the vacuum, provided that their energy exceeds the electron work function. **Figure 12** shows the measured emission efficiency (the ratio of vacuum-emitted electron current to tunneling current) as a function of the thickness of a vacuum-deposited Al gate. As expected, we see an exponential dependence, with the emission efficiency dropping off rapidly for thicker films. But even at a gate thickness of 20 nm some electrons are emitted. Below a thickness of 2 nm, the vacuum-deposited Al films are no longer continuous.

The electrons emitted into the vacuum are much like photo-emitted electrons in a PEEM experiment. They can be captured by the LEEM objective lens and used to form an image of the sample [20]. What we obtain is a spatially resolved image of the electron tunneling probability. For a defect-free oxide of uniform thickness, this image is rather boring, because it is devoid of any contrast. But when defects form, either extinguishing or enhancing the tunneling, the image becomes quite interesting. Illustratively, **Figure 13** shows a "hot-electron emission" image of a 7-nm-thick gate oxide, with a 20-nm-thick Al film, stressed at 8 V. There are numerous bright spots in the image, indicative of the formation of defects in the film. The emission intensity is much brighter in these small regions (estimated to be smaller than 50 nm), and the intensity is not constant. Some bright spots appear momentarily and disappear again. Other bright spots flare up and emit a more or less stable current for many minutes. Inspection with mirror electron microscopy (MEM) and with scanning electron microscopy (SEM) shows that these defects are associated with small

extrusions on the surface [20]. Electrical measurements show an increased leakage current at low bias voltage. We also find that these defects are formed not only during observations in the LEEM, but also in air and in the SEM, apparently independent of the environment. **Figure 14** shows an SEM image of such extrusions. It appears that the underlying Si has broken through the oxide as well as the Al gate, and is exposed to the vacuum. We speculate that these defects arise because of a strongly increased, localized tunneling current at a microscopic defect, which gives rise in turn to electromigration of Si through the oxide and the gate! Clearly, such a defect would suffice to cause a device failure.

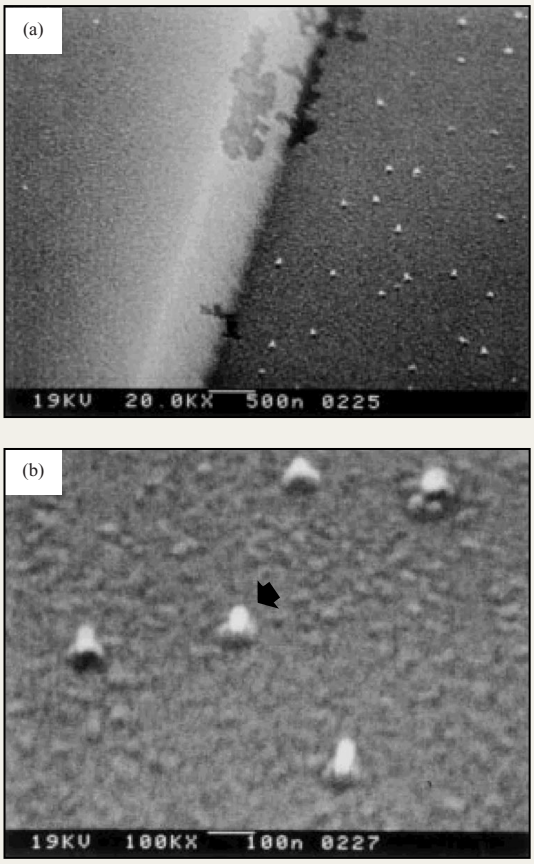

Figure 14

SEM image of a sample similar to that of Figure 13, after electrical stressing. The oxide to the left in (a) is a thick oxide; the oxide to the right is thin. Breakdown features are seen only in the thin region. As indicated in part (b), breakdown appears to give rise to localized extrusion of Si and Al, possibly by electromigration, at sites similar to the hot spots of Figure 13.

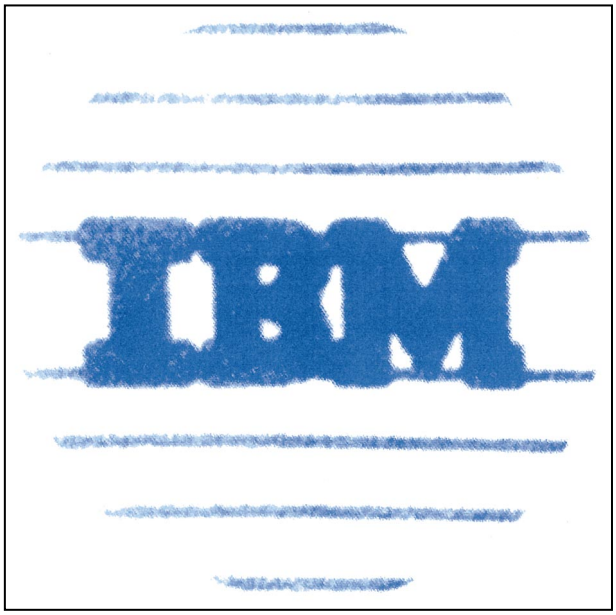

Figure 15

Hot-electron emission image of a pattern ("IBM") produced in a gate metal layer deposited using a shadow mask. The letters and bars correspond to relatively thin gate metal regions where the magnitude of electron emission is greater.

- *Hot-electron emission lithography (HEEL)*

As noted above, the electron emission current depends strongly on the thickness of the Al gate. If the gate thickness is patterned, the MOS structure can be made to function as a patterned electron emitter. For example, **Figure 15** shows an emission pattern from a sample on which the gate thickness was patterned to spell the letters IBM. The gate was deposited through a shadow mask, and the features in the image are not particularly small, but it nevertheless shows the principle. There is, however, a disadvantage to patterning the gate metal. Tunneling occurs over the entire structure, including those areas where the metal is thick, and electron emission is not desired. If the oxide thickness is patterned instead, electron tunneling occurs according to the Fowler–Nordheim mechanism and depends exponentially on oxide thickness. Thus, electron tunneling through a 5-nm-thick oxide should be 12 orders of magnitude greater than that through a 20-nm-thick oxide, leading to excellent contrast. This is indeed found to be the case, and emission features can be resolved with a resolution down to 0.05 μm.

Lithography is another bottleneck that is at the horizon of semiconductor manufacturing, and we are approaching that horizon rapidly. Ultraviolet optical lithography may be extendable to 0.1 μm, but smaller feature sizes will

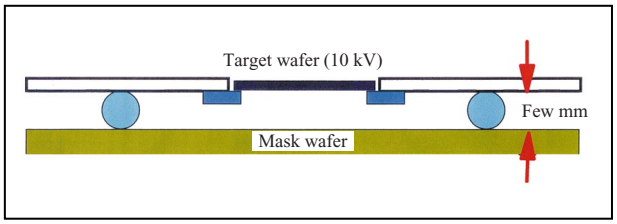

Figure 16

Schematic diagram of hot-electron emission lithography 1:1 projection scheme. The target wafer is biased positively relative to the mask (see inset in Figure 12), giving rise to a strong uniform electrostatic field between mask and wafer. A parallel magnetic field is overlapped with the electrostatic field by a large external magnet, making it possible to form a 1:1 image of the mask onto the target.

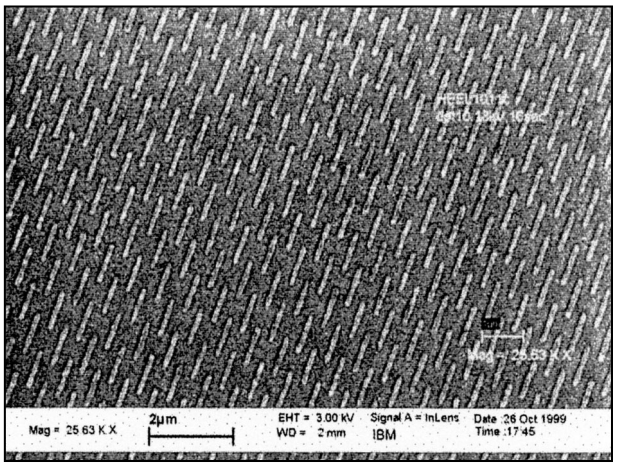

Figure 17

Image of 0.1-μm features, printed into an e-beam resist layer by the use of hot-electron emission.

require a fundamentally different technology. The obvious choices are X-rays, extreme ultraviolet (13 nm) radiation, ions, or electrons. All of these options have problems. X-ray lithography [39] has a long history, with significant investments, development, and experience within IBM and elsewhere. A thin membrane shadow mask is held in close proximity to the wafer as it is exposed to X-rays. Resolution is excellent, but the mask is fragile, subject to distortions, and not easily amenable to changes in magnification. Extreme ultraviolet (EUV) lithography [40] overcomes some of these objections, but requires fully reflective optics, with a quality of the optical components that has not been realized previously. Although several companies and government agencies have initiated an ambitious development program, the future of EUV is uncertain, and many basic questions remain unanswered. The use of ions for lithography [41] finds strong support in Europe. It requires the use of so-called stencil masks which are ion-optically demagnified onto the wafer. The mask technology is complex, and remains largely unproven. By far the most completely developed is electron lithography. Electron-beam lithography is used extensively today for mask fabrication, but because present electron-beam tools write one pixel at a time, full-wafer patterning is too time-consuming to be acceptable in semiconductor manufacturing. Several development projects aim at systems with numerous electron beams traveling down the optical columns simultaneously to reduce the total write time. Other approaches (most notably the Scalpel project [42] at Lucent Technologies and the Prevail project [43] at IBM) aim to improve writing speed by projecting significant portions of the chip at once, rather than a single pixel at a time. While these approaches promise throughputs in the range of 40 wafers per hour at 0.15-μm resolution, further improvements in resolution may reduce throughput. Also, the mask technology is quite complex, and subfields must be stitched together during wafer exposure.

Patterned electron emitter structures would seem to be promising for applications in electron lithography [44]. To demonstrate the applicability of such hot-electron masks, we have developed a simple 1:1 projection system to assess the feasibility of the general concept and examine the resolution that might be achievable. A schematic view of the projection system is shown in **Figure 16**. Basically, emission mask and wafer are held at a fixed spacing of a few mm. The wafer is biased +10 kV relative to the mask, to accelerate the electrons before they strike the e-beam resist on the wafer. A uniform magnetic field **B** is superimposed onto this electric field **E**, with **E** parallel to **B**. With the proper combination of field strengths, an electron emitted from the hot-electron mask returns to the same magnetic field line from which it originated, just where this field line intersects the sample. Thus, use of the combined electric and magnetic fields makes it possible to form a 1:1 image. At a spacing of 5 mm, the ultimate spatial resolution is 0.09 nm for the measured energy and angular spread of the emitted electrons. Even in this simple projection system we realize a resolution better than 0.15 μm, close to the theoretical resolution [21]. The resolution depends directly on the field strengths. Reduction of the spacing to 2.5 mm at a fixed wafer potential of 10 keV improves the resolution to better than 0.05 μm. We have recently implemented this improved resolution in our projection system.

Figure 17 shows an image of 0.1-μm features printed in e-beam resist, displaying excellent definition and

uniformity. Such hot-electron emission lithography (HEEL) has several distinct advantages. It can project large fields, even up to a complete chip. The exposure time is short, of the order of one second. Small adjustments in magnification are possible in a 1:1 projection system. The expected lifetimes of the electron masks are reasonable, of the order of 300 000 exposures. And the masks needed can be fabricated using standard MOS technology on conventional Si wafers. We are at present pursuing further studies on the possibilities, advantages, and disadvantages of HEEL.

Discussion and conclusions

Like most of the other emerging analytical techniques discussed in this issue, the LEEM project was conceived and started as a basic science effort. The Si(113) phase-transition study is a good example of such an effort, utilizing the unique strengths of LEEM to investigate a phenomenon that could not be studied in such detail and in this parameter space previously. But it did not take long before LEEM was being applied to more technologically oriented problems such as the growth of Ge and SiGe on Si. Finally, we have shown how the study of electron emission from MOS capacitors, aimed at obtaining insight in the spatio-temporal characteristics of gate oxide breakdown, has given rise to HEEL, a new, promising method that may make it possible to achieve high-throughput, high-resolution electron-beam lithography.

In the last few years we have worked hard to make our IBM LEEM technology available to the academic community outside IBM. Instruments can now be found at the University of Wisconsin at Madison [45] and at the University of Illinois at Urbana–Champaign [46], used in studies of Si/Ge growth, GaN growth, and thin epitaxial metal films on insulator substrates, broadening the application of LEEM in additional areas of interest. Efforts to commercialize the LEEM-II instrument are underway. Already LEEM has made major contributions to science and technology, and we consider it important to help it facilitate that, both inside and outside IBM.

Acknowledgments

For their many contributions to the work presented here, I would like to thank N. Bartelt, E. Cartier, M. Copel, A. Denier van der Gon, A. Ellis, M. Mankos, M. Poppeiler, M. Reuter, and W. Theis.

References

1. E. Bauer, in *Electron Microscopy*, Vol. 1, S. S. Breese, Ed., Academic Press, Inc., New York, 1962, p. D-11.
2. W. Telieps and E. Bauer, *Ultramicrosc.* **17,** 57 (1985).
3. R. M. Tromp and M. C. Reuter, *Ultramicrosc.* **36,** 99 (1991).
4. K. Takayanagi, Y. Tanishiro, M. Takahashi, and S. Takahashi, *J. Vac. Sci. Technol. A* **3,** 1502 (1985).
5. R. M. Tromp, R. J. Hamers, and J. E. Demuth, *Phys. Rev. Lett.* **55,** 1303 (1985).
6. H. C. Poon, S. Y. Tong, W. F. Chung, and M. S. Altman, *Surf. Rev. Lett.* **5,** 1143 (1998), and references therein.
7. R. M. Tromp, A. W. Denier van der Gon, F. K. LeGoues, and M. C. Reuter, *Phys. Rev. Lett.* **71,** 3299 (1993).
8. R. M. Tromp, M. C. Reuter, and F. K. LeGoues, *Phys. Rev. Lett.* **74,** 2706 (1995).
9. E. Bauer, *Surf. Sci.* **299/300,** 102 (1994).
10. L. H. Veneklasen, *Ultramicrosc.* **36,** 76 (1991).
11. R. M. Tromp, M. Mankos, M. C. Reuter, A. W. Ellis, and M. Copel, *Surf. Rev. Lett.* **5,** 1189 (1998).
12. R. M. Tromp and M. C. Reuter, *Ultramicrosc.* **50,** 171 (1993).
13. K. Grzelakowski and E. Bauer, *Rev. Sci. Instrum.* **67,** 742 (1996).
14. W. Engel, doctoral thesis, Freie Universitaet, Berlin, Germany, 1968.
15. G. D. Archard and T. Mulvey, *J. Sci. Instrum.* **35,** 279 (1958).
16. V. Kolarik, M. Mankos, and L. Veneklasen, *Optik* **87,** 1 (1991).
17. R. Degenhardt, doctoral thesis, Technische Hochschule Darmstadt, Germany, 1992.
18. R. M. Tromp, W. Theis, and N. C. Bartelt, *Phys. Rev. Lett.* **77,** 2522 (1996).
19. R. M. Tromp and M. C. Reuter, *Phys. Rev. Lett.* **68,** 954 (1992).
20. M. Mankos, R. M. Tromp, M. C. Reuter, and E. Cartier, *Phys. Rev. Lett.* **76,** 3200 (1996).
21. M. Poppeller, E. Cartier, and R. M. Tromp, *Appl. Phys. Lett.* **73,** 2835 (1998).
22. J. Dabrowski, H.-J. Muessig, and G. Wolff, *Phys. Rev. Lett.* **73,** 1660 (1994).
23. Y.-N. Yang, E. D. Williams, R. L. Park, N. C. Bartelt, and T. L. Einstein, *Phys. Rev. Lett.* **64,** 2410 (1990).
24. D. L. Abernathy, R. J. Birgeneau, K. I. Blum, and S. G. J. Mochrie, *Phys. Rev. Lett.* **71,** 750 (1993).
25. H. E. Stanley, *Introduction to Phase Transitions and Critical Phenomena*, Oxford Press, New York, 1971.
26. S. Tang and D. P. Landau, *Phys. Rev. B* **36,** 567 (1987).
27. M. Copel, *IBM J. Res. Develop.* **44,** 571 (2000, this issue).
28. M. Copel, M. C. Reuter, E. Kaxiras, and R. M. Tromp, *Phys. Rev. Lett.* **63,** 632 (1989).
29. N. Pinto, F. Tombolini, R. Murri, M. De Crescenzi, M. Casalboni, G. Barucca, and G. Majni, *J. Lumin.* **80,** 509 (1998).
30. D. Reinking, M. Kammler, N. Hoffmann, M. Horn Von Hoegen, and K. R. Hofmann, *Electron. Lett.* **35,** 503 (1999).
31. F. M. Ross, *IBM J. Res. Develop.* **44,** 489 (2000, this issue).
32. J. E. Cunningham, K. W. Goossen, W. Jan, and M. D. Williams, *J. Vac. Sci. Technol. B* **13,** 646 (1995).
33. H. D. Jung, N. Kumagai, T. Hanada, E. Kurtz, Z. Zhu, and T. Yao, *J. Cryst. Growth* **184–185,** 223 (1998).
34. W. F. Egelhoff, *Surf. Sci.* **402–404,** 32 (1998).
35. M. Kamiko, R. Furukawa, K. Y. Kim, M. Iwanami, and R. Yamamoto, *J. Magn. Magn. Mater.* **198–199,** 716 (1999).
36. D. A. Walters, B. L. Smith, A. M. Belcher, G. T. Paloczi, G. D. Stucky, D. E. Morse, and P. K. Hansma, *Biophys. J.* **72,** 1425 (1997).
37. J. H. Stathis and D. J. DiMaria, *Microelectron. Eng.* **48,** 395 (1999).
38. A. Delong and V. Kolarik, *J. Vac. Sci. Technol. B* **7,** 1422 (1989).
39. A. A. Krasnoperova, R. Rippstein, A. Flamholz, E. Kratschmer, S. Wind, C. Brooks, and M. Lercel, *Proc. SPIE* **3676,** 24 (1999).
40. A. M. Hawryluk, N. M. Ceglio, and D. A. Markle, *Solid State Technol.* **40,** 151 (1997).
41. A. Ehrmann, R. Kasmaier, and H. Loschner, *Proc. SPIE* **3665,** 69 (1999).
42. L. R. Harriott, *J. Vac. Sci. Technol. B* **15,** 2130 (1997).
43. H. C. Pfeiffer and W. Stickel, *Microelectron. Eng.* **27,** 143 (1995).

44. M. Poppeiler, E. Cartier, and R. M. Tromp, *Microelectron. Eng.* **46,** 183 (1999).
45. P. Sutter and M. G. Lagally, *Phys. Rev. Lett.* **82,** 1490 (1999).
46. W. Swiech, M. Mundschau, and C. P. Flynn, *Appl. Phys. Lett.* **74,** 2626 (1999).

Received January 7, 2000; accepted for publication February 28, 2000

Rudolf M. Tromp *IBM Research Division, Thomas J. Watson Research Center, P.O. Box 218, Yorktown Heights, New York 10598 (rtromp@us.ibm.com).* Dr. Tromp received a Ph.D. in physics from the University of Utrecht (The Netherlands) in 1982, after having completed a thesis on medium-energy ion scattering (MEIS) studies of the structure of silicon surfaces. In 1983 he joined IBM at the Thomas J. Watson Research Center, where his scanning tunneling microscopy studies revealed the Si(001) dimer structure for the first time, as well as the spatial distribution of the Si(111) (7×7) electronic surface states and their relation to the underlying atomic structure. Using MEIS he co-invented "surfactant-mediated epitaxial growth," a technique which allows much-improved control over the morphology of epitaxial films and superlattices. More recently, his studies have focused on the dynamics of surface and interface processes such as phase transitions, chemisorption and etching, epitaxial growth, and aspects of nanotechnology. Ultrahigh-vacuum transmission electron microscopy and low-energy electron microscopy allow detailed, real-time, *in situ* observations of such processes with high spatial resolution. Using those techniques, the studies have shed new light on the thermodynamics of epitaxial growth, the dynamic evolution of the surface morphology of epitaxial films, the self-assembly of quantum dots, the spatio-temporal character of first- and second-order phase transitions at surfaces, etc. Currently Dr. Tromp manages the Analytical Sciences Department at the Thomas J. Watson Research Center. He is the recipient of the Wayne B. Nottingham Prize of the Physical Electronics Conference (1981), the Materials Research Society Medal (1995), and three IBM Outstanding Innovation and Technical Achievement Awards. Dr. Tromp is a Fellow of the American Physical Society and of the Boehmische Physical Society. He is the holder of five U.S. patents and has published extensively in the technical literature.